Solid Earth Discuss., 7, 3053–3085, 2015
www.solid-earth-discuss.net/7/3053/2015/
doi:10.5194/sed-7-3053-2015

Solid Earth Discussions
Open Access
EGU

Eruptive shearing of tube pumice: pure and simple

D. B. Dingwell[1], Y. Lavallée[2], K.-U. Hess[1], A. Flaws[1], J. Marti[3], A. R. L. Nichols[4], H. A. Gilg[5], and B. Schillinger[6]

[1]Earth and Environmental Sciences, Ludwig-Maximilians-Universität, Theresienstr. 41/III, 80333 München, Germany
[2]Earth, Ocean and Ecological Sciences, University of Liverpool, Liverpool, UK
[3]Consejo Superior de Investigations Cientificas, Institute of Earth Sciences Jaume Almera, Barcelona, Spain
[4]Research and Development Center for Ocean Drilling Science, Japan Agency for Marine Earth Science and Technology (JAMSTEC), 2-15 Natsushima-cho, Yokosuka, Kanagawa 237-0061, Japan
[5]Lehrstuhl für Ingenieurgeologie, Ingenieursfakultät Bau Geo Umwelt, Technische Universität München, München, Germany
[6]Forschungsreaktor FRM-II, Technische Universität München, Garching, Germany

Received: 31 July 2015 – Accepted: 24 August 2015 – Published: 3 November 2015

Correspondence to: Y. Lavallée (ylava@liv.ac.uk)

Published by Copernicus Publications on behalf of the European Geosciences Union.

Abstract

Understanding the physico-chemical conditions extant and mechanisms operative during explosive volcanism is essential for reliable forecasting and mitigation of volcanic events. Rhyolitic pumices reflect highly vesiculated magma whose bubbles can serve as a strain indicator for inferring the state of stress operative immediately prior to eruptive fragmentation. Obtaining the full kinematic picture reflected in bubble population geometry has been extremely difficult, involving dissection of a small number of delicate samples. The advent of reliable high-resolution tomography has changed this situation radically. Here we demonstrate via the use of tomography how a statistically powerful picture of the shapes and connectivity of thousands of individual bubbles within a single sample of tube pumice emerges. The strain record of tube pumice is dominated by simple shear (not pure shear) in the late deformational history of vesicular magma before eruption. This constraint in turn implies that magma ascent is conditioned by a velocity gradient at the point of origin of tube pumice. Magma ascent accompanied by simple shear should enhance high eruption rates inferred independently for these highly viscous systems.

1 Introduction

Upon nucleation, bubbles may grow, deform (stretch/collapse), coalesce and burst (Proussevitch and Sahagian, 1998; Proussevitch et al., 1993). This spectrum of behaviour expresses the variable state of stress in the magma column (Rust et al., 2003), and controls the evolution of the permeable porous network (Ashwell et al., 2015; Caricchi et al., 2011; Kendrick et al., 2013; Lavallée et al., 2013; Okumura et al., 2008; Pistone et al., 2012; Rust and Cashman, 2004; Wright et al., 2006; Wright and Weinberg, 2009), which regulates degassing, and thus internal pressure build-up required for fragmentation (Rust and Cashman, 2011; Sahagian, 1999). Detail of the porous network in volcanic conduits is conventionally inferred from the characteristics of explosive

SED
7, 3053–3085, 2015

eruptive products frozen-in upon fragmentation at the glass transition. This information has enabled the elaboration of elegant, magma ascent models, including mechanical strain simulations (Neuberg et al., 2006; Papale, 1999), permeable, porous network models (Collinson and Neuberg, 2012; Klug and Cashman, 1996) and fragmentation criteria (Koyaguchi et al., 2008; Spieler et al., 2004). Of all volcanic products, tube pumices (also termed fibrous or woody pumices) display one of the most spectacular, porous network configurations (e.g., Wright et al., 2006). Their enigmatic structure is made up of a collated amalgamation of elongate bubbles separated by extremely thin glassy walls. In fact, the remarkably delicate structure of tube pumices questions our understanding of the kinetics underlying volcanic eruptions at the point of fragmentation of such particular bubble-rich magmas.

Tube pumices have been postulated to offer a unique strain marker of the ductile-brittle processes enacted at fragmentation (Marti et al., 1999). Yet, the dilemma posed by tube pumices is that of stress and strain distribution inside volcanic conduits (Fig. 1). Fundamentally, do pores stretch due to pure shear or simple shear? Such contrasting strain mechanistics may underline equally contrasting magma ascent dynamics. For instance, pure shear may be favoured in a regime where the strain induced by magma ascent acceleration exceeds the bubble growth rate associated by volatile exsolution (Mader et al., 1996). Alternatively, simple shear may be favoured in a regime where velocity gradient in areas of strain localisation along the conduit margin may stretch bubbles (Polacci, 2005). Thus the mechanisms causing tube pumice hold key tensorial information necessary to assess conduit flow mechanics. To resolve this dispute, we employ capabilities recently gained through advances in neutron computed tomography to reconstruct the porous network of tube pumice in unprecedented detail.

2 Tube pumice of the Ramadas Volcanic Centre

The Ramadas Volcanic Complex (RVC) is located in the Altiplano-Puna Plateau of the Central Andes, in NW of Argentina (Casas et al., 1995; Gauthier et al., 1994; Marti

SED
7, 3053–3085, 2015

et al., 1999; Tait et al., 2009; Viramonte et al., 1984), near the township of San Antonio de los Cobres (Fig. 2a). Formed 8.7 Ma ago, the RVC is composed of a 4 km × 3 km amphitheatre defined by the remains of rhyolitic domes and proximal pyroclastic deposits, set within uplifted Precambrian–Lower Cambrian meta-sedimentary rocks of the Puncoviscana Formation, and a widespread sequence of pyroclastic deposits mostly emplaced to the east from that vent area. Due to a lack of clear and continuous exposure, the vent boundaries are largely inferred from facies relationships (Tait et al., 2009; Viramonte et al., 1984) and geophysical gravimetric modelling (Casas et al., 1995).

Recent studies suggest that the Ramadas pyroclastic deposits were produced during an extremely explosive, Plinian scale eruption from a flaring point source vent structure (Tait et al., 2009). The RVC has erupted a complex suite of rhyolitic pyroclastic and coherent volcanic rocks, dominated by thick, Plinian pumice fall deposits, with subordinate intercalated pyroclastic surge and ignimbrite deposits, representing more than 35 km^3 (DRE) of juvenile material (Tait et al., 2009). A particular characteristic of the Ramadas pumice fall deposits is the presence of abundant tube pumices (Fig. 2b).

The pumices are composed of angular lapilli with a texture composed of tubular bubbles (Marti et al., 1999). The porosity of the undeformed pumice has been estimated at 49–64 %, whereas the tube pumice reach 63–78 % (Marti et al., 1999). The stretched nature of tube pumice pores exhibit variable connectivity achieving an anisotropic permeability ranging from $\sim 10^{-8}$ m^2 along the stretching axis to 10^{-13} m^2 in the orthogonal direction (Wright et al., 2006). Up to 40 % of the tube pumice exhibit localised kink bands, or box folds, characterised by couples of parallel dextral and sinistral shear planes, crosscutting the main pore structure at an angle of 45° (Marti et al., 1999) and thus providing evidence of a late-stage deformation.

All pumices present in the deposits show very similar morphological and textural characteristics – in terms of bubble size, maximum stretching of bubbles, thickness of the bubble walls – at both, macroscopic and microscopic scales. The sample investigated below comes from a population of 200 samples that which correspond to the most pristine of all the samples collected in 5 field seasons between 1985 and 2009.

SED
7, 3053–3085, 2015

These 200 samples were selected because they were not partially altered or devitrified due to post-depositional processes. The sample analysed in this study is highly representative of the eruptive products in these highly homogeneous deposits of Ramadas volcano. There is no significant textural variability apart from the existence of the shear deformation in some of them, already described. The remarkable constancy of the kinematic features of the Ramadas tube pumices is in fact what makes this choice of pumice so especially appropriate for the analysis and conclusions presented in the present study.

3 Chemical properties of tube pumice

Extensive petrologic characterisation of the eruptive products provides us with parameters to constrain their rheological behaviour (e.g., Gauthier et al., 1994). The Ramadas fallout pumices are peraluminous rhyolite (Table 1). They are mostly aphyric, but the minor presence of freshly preserved pyralspite garnets, have been used to constrain starting pre-eruptive conditions to 250–300 MPa and 860–875 °C (Gauthier et al., 1994). The rheological analysis described below requires first a detailed understanding of water concentration present in the melt at the point of fragmentation. This was achieved via a combination of Fourier transform infrared analysis (FTIR) and stable hydrogen and oxygen isotope analysis.

3.1 Water speciation in the Ramadas pumice

The water content present in the tube pumice was quantified via micro-FTIR spectroscopy using a Varian FTS Stingray 7000 Micro Image Analyzer spectrometer at the Institute for Research on Earth Evolution (IFREE), Japan Agency for Marine Earth Science and Technology (JAMSTEC). Spectra were collected over 512 scans at a resolution of 8 cm^{-1} using a heated ceramic (globar) infrared source and a Ge-coated KBr beamsplitter. A UMA 600 microscope was coupled to the spectrometer to permit pre-

SED
7, 3053–3085, 2015

cise focusing of the beam on the area of interest. The beam path within the spectrometer bench and microscope was continuously purged with N_2 gas and the laboratory was kept as dry as possible to minimize any interference from the atmosphere. The glass shards were placed on a H_2O-free IR-invisible KBr disk, for which background analyses had been taken. For spot analyses, a liquid-nitrogen cooled $HgCdTe_2$ (MCT) detector was used, and the aperture was 50 µm^2. This set up permitted collection of spectra across the mid-IR region (6000–700 cm^{-1}). Some spectra were also extracted from 350 µm × 350 µm spectroscopic images, which were collected following the same procedure as the conventional spot analyses except for the detector, which was a Varian Inc. Lancer Focal Plane Array (FPA) camera. The FPA camera consists of a MCT array detector with 4096 channels (64 × 64), which collect spectra over the spectral range 4000–900 cm^{-1}. This setup offers a channel (or spectral) resolution of 5.5 µm. Any of the 4096 spectra from the image could be extracted for individual treatment. (For a more detailed discussion of spectroscopic imaging and the set up see Wysoczanski and Tani, 2006).

The perfect plane-parallel nature of tube pumices' bubble walls mean that the fragmented glass shards require minimal sample preparation to meet the requirements to be able to conduct micro-FTIR spectroscopy. Two samples were selected for image and spot ($n = 25$) FTIR analysis. Absorbance at the 1628 and 3567 cm^{-1} peaks was used to derive molecular H_2O contents (hereafter termed H_2O_m) and total H_2O content (hereafter termed H_2O_t) that includes H_2O_m as well as OH^- species using the modified Beer–Lambert law:

$$c_i = \frac{M_i \cdot A}{\rho \cdot t \cdot \varepsilon}, \quad (1)$$

where c_i is the concentration of the species i (in wt. %), M_i is the molecular weight of the species of i (g mol^{-1}), A is the absorbance of the relevant vibration band, ρ is the sample density (g L^{-1}), t is the thickness of the area analysed (cm), and ε is the molar absorptivity (L mol^{-1} cm^{-1}). Absorbance was measured as the height of the peaks

SED
7, 3053–3085, 2015

above a linear baseline. Sample density was calculated from the oxide composition of the glass, measured by electron probe micro-analysis (e.g., Lange, 1997). The thickness of the glass shards were estimated optically using a Zeiss micrometer. Molar absorptivity coefficients of 55 $L\,mol^{-1}\,cm^{-1}$ (Newman et al., 1986) for the 1628 cm^{-1} H_2O_m peak and 90 $L\,mol^{-1}\,cm^{-1}$ (Hauri et al., 2002) for the 3567 cm^{-1} H_2O_t peak were used.

Volatile distribution images obtained with the FPA camera reveal the homogeneity of water speciation (Fig. 3). Thin bands with higher concentration are where a second bubble wall, orthogonal to the plane of view, intersects the main bubble wall. Computation of the water speciation indicates the presence of 4.78–5.49 wt. % H_2O_t of which ~ 85 % is molecular (Table 2). When compared to the equilibrium model of water speciation for rhyolite compositions (Zhang, 1999), the obtained water concentration (Fig. 4) shows disequilibrium which suggests post-emplacement hydration by meteoric water (e.g., Denton et al., 2009). In order to confirm this we analysed the oxygen and hydrogen isotope compositions of the samples, which also provides further information on the origin of the meteoric water.

3.2 Stable H and O isotope in Ramadas pumice

Stable isotope measurements on two tube pumice samples, one unaltered and the other slightly weathered, were performed at University of Lausanne, Switzerland. Hydrogen isotope compositions were determined using a high-temperature (1450 °C) reduction method with He carrier gas and a TC-EA linked to a Delta Plus XL mass spectrometer from Thermo–Finnigan on 2 to 5 mg sized samples (Sharp et al., 2001). Each sample was measured three times. Hydrogen contents were calculated from hydrogen voltage signals, sample weights, and a calibration curve, and are expressed as weight percent water. They have an accuracy of about ±0.08 wt. % H_2O. Oxygen was extracted from 0.5 to 2 mg of sample by heating with a CO_2-laser in a F_2 atmosphere of 50 mbar (Kasemann et al., 2001; Sharp, 1990). An overnight prefluorination step was conducted to remove easy exchangeable, surface-bound water. The extracted O_2 was collected on a molecular sieve (5 Å) and subsequently expanded into a Finnigan MAT

SED
7, 3053–3085, 2015

253 dual-inlet isotope ratio mass spectrometer. The results are given in the standard δ-notation expressed relative to Vienna standard mean ocean water (VSMOW) in per-mil (‰). The accuracy was better than ±2 ‰ for hydrogen and better than ±0.2 ‰ for oxygen isotope analyses.

The fresh tube pumice sample has a $\delta^{18}O_{VSMOW}$ value of 14.0 ‰ and δD_{VSMOW} values are −129 ± 2 ‰, while the slightly weathered sample is somewhat isotopically lighter with 13.1 ± 0.2 ‰ for oxygen and −135 ± 2 ‰ for hydrogen isotope values (Table 3). The water contents are 4.85 wt. % for the fresh and 5.00 wt. % for the slightly weathered sample. The oxygen and hydrogen isotope data are not consistent with an undegassed primary magmatic isotope signature (Goff and McMurtry, 2000; Sheppard et al., 1969). They plot in a $\delta^{18}O$–δD diagram (Fig. 5) close to the hydrated volcanic glass line (HVGL) of Taylor (1968). This line corresponds to isotope compositions of hydrated acidic glasses in equilibrium with meteoric waters at low temperatures (~ 20 °C). We note that this does not necessarily imply that anhydrous glasses were hydrated at ambient temperatures (Cerling et al., 1985; Taylor, 1968). It is possible that glasses that were hydrated at high temperatures and re-equilibrated with meteoric waters at low temperatures due to diffusive isotope exchange over time scales of tens of thousand to about one million years (Gilg and Sheppard, 1999). The isotope composition of waters on the global meteoric water line in equilibrium the two glass samples can be calculated using the equilibrium isotope fractionation factors of Taylor (1968) and Friedman et al. (1993) and are −12 ‰ for $\delta^{18}O$ and −90 ‰ for δD (Fig. 5). These values are higher than the local average meteoric waters at an elevation of about 3800 m a.s.l. (~ −15 ‰/ − 110 ‰; Fernández et al., 1991; Hoke et al., 2009; Quade et al., 2007; Sharp et al., 2003). This difference indicates the glasses were isotopically equilibrated at lower elevations than they are at today, consistent with the uplift history of the Altiplano (Garzione et al., 2008).

SED
7, 3053–3085, 2015

3.3 Magmatic water content at fragmentation

Concluding that most of the water measured in the pumice is derived from post-eruption hydration by meteoric waters, we turn to the water speciation equilibrium law for rhyolite compositions (i.e., Zhang, 1999) in order to estimate the original magmatic water content. Post-eruption hydration is believed to add molecular water without altering the concentration of the OH-group locked in the structure of a glass (Denton et al., 2009). Thus we can use the concentration of OH^- species to extrapolate the total magmatic molecular water assuming equilibrium speciation (Fig. 6). Here, The OH^- species concentration of 0.69–0.78 wt. % is used in the water speciation equilibrium law of Zhang (1999) to constrain a total magmatic water content of approximately 0.86–1.01 wt. %, which could indicate a pressure as low as 10 MPa. Given the likely possibility of isotopic exchange with a higher initially magmatic water content, together with the extreme degassing conditions extant during the formation of tube pumice, we infer significantly higher water contents that this minimum estimate during the shearing flow described here. Together with the geochemical composition provided by Gauthier (1994), the water concentration can be used as first order constraint for the calculation of the rheological properties of the tube pumice necessary at the point of fragmentation to constrain the underlying shearing regime.

4 Porous network analysis

Advance in non-destructive tomographic imaging has provided us with a key tool to detail the internal porous structure of volcanic rocks (Ashwell et al., 2015; Bai et al., 2011; Baker et al., 2012; Degruyter et al., 2010; Lavallée et al., 2013; Okumura et al., 2008; Wright et al., 2006). Here, the internal structure of the tube pumice was imaged in 3-D using neutron computed tomography the ANTARES beamline (FRM-II) in Garching, Germany (Hess et al., 2011). 800 single radiographs were taken by rotating the sample each time by 0.45° with an exposure time of 50 s at a collimation of 800

SED
7, 3053–3085, 2015

(ratio of beam flight length to pinhole diameter). The neutron beam interaction with the sample was detected by a 100 µm thick neutron sensitive scintillation screen (ZnS + LiF). The resulting set of radiographs was then reconstructed using the inverse radon transformation (Deans, 2007) to generate a 3-D image of the local attenuation within the object with a voxel size 51.2^3 µm^3 (Fig. 7).

The resulting dataset (> 12 000 bubbles) was then segmented using a watershed algorithm acting on the attenuation gradient in order to accurately map the pores' size, shape and orientation (Fig. 7; see Supplement). Except where the bubble coalesced (which were discarded for the analysis below), bubble walls are generally observed to form a perfectly closed shell around each pore (Fig. 7c–e). The pores were characterised in terms of their volumes, aspect ratio (l/a), ellipticity ($1 - c/b$), orientation (θ) and undeformed radius (a) (Fig. 8). Each pore was characterised using a least-squares ellipsoid fit. This fitting was performed in an automatic fashion using the labelled regions and edges determined by the segmentation algorithm. The quality of the fitting was manually evaluated by overlaying the fitted ellipsoid and edge voxels. Poor ellipsoid fits, often due to bubble coalescence, were excluded.

The observed geometry of the pore space was numerically modelled to constrain the conditions of strain rate in the conduits. The steady shapes and orientations of bubbles in a viscous Newtonian fluid deforming via simple or pure shear can be expressed as a function of the capillary number (Ca):

$$\mathrm{Ca} = \frac{aG\mu_\mathrm{s}}{\Gamma}, \tag{2}$$

where a is the undeformed bubble radius, and G, μ_s and Γ are the shear rate, the shear viscosity and the surface tension of the magma, respectively. The undeformed bubble radius is calculated from the voxel volume of each pore (V) via

$$a = \left(\frac{3}{4\pi}V\right)^{1/3}, \tag{3}$$

SED
7, 3053–3085, 2015

Yet, the reconstructed bubbles preserved in the tube pumice may not directly reflect the bubbles present in the conduit upon fragmentation; that is, after fragmentation, the liquid in the bubble walls may have some time to relax and the bubble may regain a spherical shape before the eruptive products freeze in at the glass transition. The effect of relaxation on bubble radius has been experimentally determined to be:

$$\frac{\ell - a}{\ell_i - a} = \exp\left(\frac{-0.67\Gamma t}{a\mu_s}\right), \quad (4)$$

where ℓ is the current major radius of the bubble and ℓ_i is the initial major radius (Rust and Manga, 2002). Although the experimental calibration of these relations have been performed at lower bulk vesicularity than is exhibited here, and potentially further aspects of bubble–bubble interactions may ensue at high vesicularities, we see in these samples no evidence of the latter. Furthermore, the precedent of applying this treatment at similar levels of vesicularities is well-established in the recent literature (Moitra et al., 2013). We note that an experimental calibration at higher vesicularities, using controlled deformation experiments is clearly a priority for the future. The surface tension at 1 kbar pressure (Bagdassarov et al., 2000) and the viscosity (Hess and Dingwell, 1996) of peraluminous silicate liquid can be expressed as functions of temperature (T) and measured total magmatic water content (w):

$$\Gamma = \frac{-11\,323.7}{T} + 179.17 \quad (5)$$

and

$$\log\mu_s = -3.545 + 0.833\ln w + \frac{9601 - 2368\ln w}{T - 195.7 - \ln w}. \quad (6)$$

In our post-fragmentation deformation analysis, we assume that the temperature of the liquid in the tube pumice follows the Newtonian cooling law,

$$T = (T_i - T_{env})\,e^{-kt} + T_{env}, \quad (7)$$

SED
7, 3053–3085, 2015

where T_i is the initial temperature (set by geothermometry at 860–875 °C), $T_{env.}$ is the temperature of the environment (20 °C), and k is the characteristic cooling rate defined by the following cooling rate experiment: a thermocouple was embedded in the center of the tube pumice block used for tomography that was then subjected to cooling from 850 °C to room temperature while recording upon removal from the furnace; using Eq. (7) the characteristic cooling rate was constrained to $10^{-4.9}$ s^{-1}. The integration of Eq. (2) through (7) provides us with the capillary number of bubbly magmas, which may be assessed for bubble orientation and deformation in pure or simple shear flows for high and low deformation regimes (Table 4; Rust et al., 2003). We ultimately obtain expressions for the evolution of bubbles' shape and orientations. Extrapolation of these expressions to an arbitrarily large time allows the shape and orientation of pores in a tube pumice formed under each shear scenario to be predicted. Note that by fixing the characteristic cooling rate, the water content remains the only free fit parameter. The results of that fitting yield water contents consistent with the discussion above.

The 3-D dataset reveals that bubble orientation with respect to the flow direction as well as the major axis length varies with the undeformed bubble radius (Fig. 9). From the mechanical scenarios that we have envisaged, the bubbles in a pure shear regime would implicitly stretch with the flow direction regardless of their initial size, whereas in a simple shear regime they would stretch according to the local stress, which will not necessarily be parallel to the flow direction. It is thus abundantly evident (Fig. 9a) that the bubble orientation matches the expected distribution from a simple shear mechanism, best constrained by a strain rate of 10^{-2} s^{-1}. Numerically, it was only possible to fit the observed bubble elongation using a simple shear model, whereas pure shear required non-physical values of strain rates and an infinitely fast cooling rate in order to fit some of the observations. In the simple shear model, we observe that internal heat transport can account for the entire data distribution (Fig. 9b). Thus the model indicates that simple shear controls the late fate of the porous network of the tube pumice immediately preceding explosive fragmentation.

SED
7, 3053–3085, 2015

5 Simple shear in volcanic conduits

The dominance of simple shear in the generation of tube pumice of the Ramadas Plinian phase, speaks of its significance in the magma column. Geometrically, we may view tube pumice as an estimate of the simple shear in the conduit flow. In a mechanistic sense, this simple shear strain, drives the extremely fast ascent rates prior to fragmentation (Castro and Dingwell, 2009). Indeed, the formation of tube pumice in marginal areas of strain localisation suggests that the principal stress was sub-parallel to flow direction and not parallel, as proposed in our previous study (Marti et al., 1999).

The preservation of kink bands forming angular box folds in the pumice further highlights the need for fluctuations in compressional deformation axial to the stretching direction of the bubbles. Whereas the stretched bubbles record the pervasive, or ductile, nature of deformation in the marginal areas of a plug flow, the kink bands, with their localised character akin to a box fold, entail a stronger and presumably shorter compressional event in the direction of a highly anisotropic medium. Here we speculate that their triggering mechanism is the very late stage passage of shock fronts generated during the explosions accompanying fragmentation, as an earlier generation of kink bands would have been subjected to further deformation and offsetting, although other unexplored mechanisms of very late stage generation might be feasible.

If tube pumices are indeed a strain marker of the ductile-brittle transition of magma upon fragmentation, they may thus provide us with the information required to reconstruct the shearing mode distribution that drives explosive eruptions. Increased simple shearing of the bubble network may eventually accentuate the permeability and vertical degassing of the magma in the conduit (Wright et al., 2006; Wright and Weinberg, 2009). The effects of such shearing in the conduit may favour a shift of the fragmentation level in the magma column to greater depths and higher pressures as has evidently been the case at Ramadas. Upon fragmentation, compressive shocks released in the marginal magmas may generate kinks, which offset the tubular bubbles and upset the degassing network, subsequently leading to fragmentation and generation of

SED
7, 3053–3085, 2015

tube pumices. We conclude that an overlying and overriding simple shear strain in magma (accompanied in this case by kink band generation) is a major regulator of ascent dynamics and fragmentation front stabilisation. Major kinematic campaigns of eruptive products will be necessary in order to perform the global comparison of eruptive dynamics unlocked by these techniques.

The Supplement related to this article is available online at doi:10.5194/sed-7-3053-2015-supplement.

Author contributions. D. B. Dingwell, K.-U. Hess, Y. Lavallée designed the experiments. K.-U. Hess and B. Schillinger performed the tomographic scans and A. Flaws analysed and modelled them. A. R. L. Nichols and Y. Lavallée analysed the water content and H. A. Gilg the isotopes composition. J. Marti performed fieldwork and collected samples. All authors contributed to the study.

Acknowledgements. We thank Thomas Shea for constructively reviewing an earlier version of this manuscript. Financial support was provided by the Deutsche Forschungsgemeinschaft (DFG) – International Continental Drilling Program (ICDP) grant HE 4565-2-1 as well as the DFG grants LA 2651-1-1 and LA 2651 3-1. Y. Lavallée acknowledges support from the European Research Council (ERC) for the Starting Grant on *Strain Localisation in Magmas* (SLiM, no. 306488). D. B. Dingwell acknowledges a Research Professorship in Experimental Volcanology of the Bundesexzellenzinitiative (LMUexcellent) as well as an ERC Advanced Grant on *Explosive Volcanism in the Earth System* (EVOKES, no. 247076).

References

Ashwell, P. A., Kendrick, J. E., Lavallée, Y., Kennedy, B. M., Hess, K. U., von Aulock, F. W., Wadsworth, F. B., Vasseur, J., and Dingwell, D. B.: Permeability of compacting porous lavas, J. Geophys. Res.-Sol. Ea., 120, 1605–1622, doi:10.1002/2014JB01151, 2015.

Bagdassarov, N., Dorfman, A., and Dingwell, D. B.: Effect of alkalis, phosphorus, and water on the surface tension of haplogranite melt, Am. Mineral., 85, 33–40, 2000.

SED
7, 3053–3085, 2015

Bai, L. P., Baker, D. R., and Hill, R. J.: Permeability of vesicular Stromboli basaltic glass: lattice Boltzmann simulations and laboratory measurements, J. Geophys. Res.-Sol. Ea., 115, B07201, doi:10.1029/2009JB007047, 2011.

Baker, D. R., Brun, F., O'Shaughnessy, C., Mancini, L., Fife, J. L., and Rivers, M.: A four-dimensional X-ray tomographic microscopy study of bubble growth in basaltic foam, Nature Communications, 3, 1135, doi:10.1038/ncomms2134, 2012.

Caricchi, L., Pommier, A., Pistone, M., Castro, J., Burgisser, A., and Perugini, D.: Strain-induced magma degassing: insights from simple-shear experiments on bubble bearing melts, B. Volcanol., 73, 1245–1257, 2011.

Casas, A., Hernandez, E., Marti, J., and Petrinovic, I.: Gravity modelling of the Ramadas Caldera (Argentinean Puna, Central Andes), 4° Congresso Internacional Da Sociedade Brasileira de Geofisica, Rio de Janeiro, Brazil, 20–24 August, 1995.

Castro, J. M. and Dingwell, D. B.: Rapid ascent of rhyolitic magma at Chaiten volcano, Chile, Nature, 461, 780–784, 2009.

Cerling, T. E., Brown, F. H., and Bowman, J. R.: Low-temperature alteration of volcanic glass: hydration, Na, K, ^{18}O and Ar mobility, Chem. Geol., 52, 281–293, 1985.

Collinson, A. S. D. and Neuberg, J. W.: Gas storage, transport and pressure changes in an evolving permeable volcanic edifice, J. Volcanol. Geoth. Res., 243, 1–13, 2012.

Compton, J. S., Conrad, M. E., and Vennemann, T. W.: Stable isotope evolution of volcanic ash layers during diagenesis of the Miocene Monterey formation, California, Clay. Clay Miner., 47, 84–95, 1999.

Deans, S. R.: The Radon Transform and Some of its Applications, Dover Publishing Co, New York, USA, 2007.

Degruyter, W., Bachmann, O., and Burgisser, A.: Controls on magma permeability in the volcanic conduit during the climactic phase of the Kos Plateau Tuff eruption (Aegean Arc), B. Volcanol., 72, 63–74, 2010.

Denton, J. S., Tuffen, H., Gilbert, J. S., and Odling, N.: The hydration and alteration of perlite and rhyolite from Iceland, J. Geol. Soc. London, 166, 895–904, 2009.

Fernández, J., Markgraf, V., Panarello, H. E., Albero, M., Angiolini, F. E., Valencio, S., and Arriaga, M.: Late Pleistocene/Early Holocene environments and climates, fauna, and human occupation in the Argentine Altiplano, Geoarchaeology, 6, 251–272, 1991.

Friedman, I., Gleason, J., Sheppard, R. A., and Gude, A. J.: Deuterium fractionation as water diffuses into silicic volcanic ash, in: Climate change and continental isotopic records, edited

SED
7, 3053–3085, 2015

by: Swart, P. K., Lohmann, K. C., McKenzie, J., and Savin, S., Geophysical Monograph, American Geophysical Union, Washington, D. C., 321–323, 1993.
Garzione, C. N., Hoke, G. D., Libarkin, J. C., Withers, S., MacFadden, B., Eiler, J., Gosh, P., and Mulch, A.: Rise of the Andes, Science, 320, 1304–1307, 2008.
Gauthier, P. J., Deruelle, B., Viramonte, J., and Aparicio, A.: Garnets from La Pava-Ramadas rhyolite (NW Argentina) and from its granite xenoliths, C. R. Acad. Sci. II, 318, 1629–1635, 1994.
Gilg, H. A. and Sheppard, S. M. F.: Stability of H and O isotope ratios in natural hydrated silicic glasses: estimation of diffusion coefficient for water at ambient temperatures, Journal of Conference Abstracts, Proceedings of EUG 10, Strasbourg, France, 28 March–1 April, 4, 531, 1999.
Goff, F. and McMurtry, G. M.: Tritium and stable isotopes of magmatic waters, J. Volcanol. Geoth. Res., 97, 347–396, 2000.
Hauri, E., Wang, J. H., Dixon, J. E., King, P. L., Mandeville, C., and Newman, S.: SIMS analysis of volatiles in silicate glasses 1. Calibration, matrix effects and comparisons with FTIR, Chem. Geol., 183, 99–114, 2002.
Hess, K. U. and Dingwell, D. B.: Viscosities of hydrous leucogranitic melts: a non-Arrhenian model, Am. Mineral., 81, 1297–1300, 1996.
Hess, K. U., Flaws, A., Muehlbauer, M. J., Schillinger, B., Franz, A., Schulz, M., Calzada, E., Dingwell, D. B., and Bente, K.: Advances in high-resolution neutron computed tomography: adapted to the earth sciences, Geosphere, 7, 1294–1302, 2011.
Hoke, G. D., Garzione, C. N., Araneo, D. C., Latorre, C., Strecker, M. R., and Williams, K. J.: Stable isotope altimeter: Do Quaternary pedogenic carbonates predict modern elevantions?, Geology, 37, 1015–1018, 2009.
Kasemann, S., Meixner, A., Rocholl, A., Vennemann, T., Schmitt, A., and Wiedenbeck, M.: Boron and oxygen isotope composition of certified reference materials NIST SRM 610/612, and reference materials JB-2G and JR-2G, Geostandard. Newslett., 25, 405–416, 2001.
Kendrick, J. E., Lavallée, Y., Hess, K. U., Heap, M. J., Gaunt, H. E., Meredith, P. G., and Dingwell, D. B.: Tracking the permeable porous network during strain-dependent magmatic flow, J. Volcanol. Geoth. Res., 260, 117–126, 2013.
Klug, C. and Cashman, K. V.: Permeability development in vesiculating magmas: implications for fragmentation, B. Volcanol., 58, 87–100, 1996.

SED
7, 3053–3085, 2015

Koyaguchi, T., Scheu, B., Mitani, N. K., and Melnik, O.: A fragmentation criterion for highly viscous bubbly magmas estimated from shock tube experiments, J. Volcanol. Geoth. Res., 178, 58–71, 2008.

Lange, R. A.: A revised model for the density and thermal expansivity of $K_2O–Na_2O–CaO–MgO–Al_2O_3–SiO_2$ liquids from 700 to 1900 K: extension to crustal magmatic temperatures, Contrib. Mineral. Petr., 130, 1–11, 1997.

Lavallée, Y., Benson, P. M., Heap, M. J., Hess, K.-U., Flaws, A., Schillinger, B., Meredith, P. G., and Dingwell, D. B.: Reconstructing magma failure and the degassing network of dome-building eruptions, Geology, 41, 515–518, 2013.

Mader, H. M., Phillips, J. C., Sparks, R. S. J., and Sturtevant, B.: Dynamics of explosive degassing of magma: observations of fragmenting two-phase flows, J. Geophys. Res.-Sol. Ea., 101, 5547–5560, 1996.

Marti, J., Soriano, C., and Dingwell, D. B.: Tube pumices as strain markers of the ductile-brittle transition during magma fragmentation, Nature, 402, 650–653, 1999.

Moitra, P., Gonnermann, H. M., Houghton, B. F., and Giachetti, T.: Relating vesicle shapes in pyroclasts to eruption styles, B. Volcanol., 75, 691–691, 2013.

Neuberg, J. W., Tuffen, H., Collier, L., Green, D., Powell, T., and Dingwell, D.: The trigger mechanism of low-frequency earthquakes on Montserrat, J. Volcanol. Geoth. Res., 153, 37–50, 2006.

Newman, S., Stolper, E. M., and Epstein, S.: Measurement of water in rhyolitic glasses – Calibration of an infrared spectroscopic technique, Am. Mineral., 71, 1527–1541, 1986.

Okumura, S., Nakamura, M., Tsuchiyama, A., Nakano, T., and Uesugi, K.: Evolution of bubble microstructure in sheared rhyolite: formation of a channel-like bubble network, J. Geophys. Res.-Sol. Ea., 113, B07208, doi:10.1029/2007JB005362, 2008.

Papale, P.: Strain-induced magma fragmentation in explosive eruptions, Nature, 397, 425–428, 1999.

Pistone, M., Caricchi, L., Ulmer, P., Burlini, L., Ardia, P., Reusser, E., Marone, F., and Arbaret, L.: Deformation experiments of bubble- and crystal-bearing magmas: rheological and microstructural analysis, J. Geophys. Res.-Sol. Ea., 117, B05208, doi:10.1029/2011JB008986, 2012.

Polacci, M.: Constraining the dynamics of volcanic eruptions by characterization of pumice textures, Ann. Geophys., 48, 731–738, 2005, http://www.ann-geophys.net/48/731/2005/.

SED
7, 3053–3085, 2015

Proussevitch, A. A. and Sahagian, D. L.: Dynamics and energetics of bubble growth in magmas: analytical formulation and numerical modeling, J. Geophys. Res.-Sol. Ea., 103, 18223–18251, 1998.
Proussevitch, A. A., Sahagian, D. L., and Kutolin, V. A.: Stability of foams in silicate melts, J. Volcanol. Geoth. Res., 59, 161–178, 1993.
Quade, J., Garzione, C., and Eiler, J.: Paleoelevation reconstruction using pedogenic carbonates, Rev. Mineral. Geochem., 66, 53–87, 2007.
Rust, A. C. and Cashman, K. V.: Permeability of vesicular silicic magma: inertial and hysteresis effects, Earth Planet. Sc. Lett., 228, 93–107, 2004.
Rust, A. C. and Cashman, K. V.: Permeability controls on expansion and size distributions of pyroclasts, J. Geophys. Res.-Sol. Ea., 116, B11202, doi:10.1029/2011JB008494, 2011.
Rust, A. C. and Manga, M.: Bubble shapes and Orientations in low Re simple shear flow, J. Colloid Interf. Sci., 249, 476–480, 2002.
Rust, A. C., Manga, M., and Cashman, K. V.: Determining flow type, shear rate and shear stress in magmas from bubble shapes and orientations, J. Volcanol. Geoth. Res., 122, 111–132, 2003.
Sahagian, D.: Volcanology – Magma fragmentation in eruptions, Nature, 402, 589–591, doi:10.1038/45099, 1999.
Sharp, Z. D.: A laser-based microanalytical method for the in-situ determination of oxygen isotope ratios of silicates and oxides, Geochim. Cosmochim. Ac., 54, 1353–1357, 1990.
Sharp, Z. D., Atudorei, V., Panarello, H. O., Fernández, J., and Douthitt, C.: Hydrogen isotope systematics of hair: archeological and forensic applications, J. Archaeol. Sci., 30, 1709–1716, 2003.
Sheppard, S. M. F., Nielson, R. L., and Taylor, H. P. J.: Oxygen and hydrogen isotope ratios of clay minerals from porphyry copper deposits, Econ. Geol., 64, 755–777, 1969.
Spieler, O., Dingwell, D. B., and Alidibirov, M.: Magma fragmentation speed: an experimental determination, J. Volcanol. Geoth. Res., 129, 109–123, 2004.
Tait, M. A., Cas, R. A. F., and Viramonte, J. G.: The origin of an unusual tuff ring of perlitic rhyolite pyroclasts: the last explosive phase of the Ramadas Volcanic Centre, Andean Puna, Salta, NW Argentina, J. Volcanol. Geoth. Res., 183, 1–16, 2009.
Taylor, B. E., Eichelberger, J. C., and Westrich, H. R.: Hydrogen isotopic evidence for rhyolitic magma degassing during shallow intrusion and eruption, Nature, 306, 541–545, 1983.

SED
7, 3053–3085, 2015

Taylor, H. P. J.: The oxygen isotope geochemistry of igneous rocks, Contrib. Mineral. Petr., 19, 1–71, 1968.

Viramonte, J. G., Omarini, R. H., Araña Saavedra, V., Aparicio, A., García Cacho, L., and Párica, P.: Edad, génesis y mecanismos de erupción de las riolitas granatíferas de San Antonio de los Cobres, Provincia de Salta, IX Congr. Geol. Arg. Actas, San Carlos de Bariloche, Argentina, 3, 216–233, 1984.

Wright, H. M. N. and Weinberg, R. F.: Strain localization in vesicular magma: implications for rheology and fragmentation, Geology, 37, 1023–1026, 2009.

Wright, H. M. N., Roberts, J. J., and Cashman, K. V.: Permeability of anisotropic tube pumice: model calculations and measurements, Geophys. Res. Lett., 33, L17316, doi:10.1029/2006GL027224, 2006.

Wysoczanski, R. and Tani, K.: Spectroscopic FTIR imaging of water species in silicic volcanic glasses and melt inclusions: an example from the Izu-Bonin arc, J. Volcanol. Geoth. Res., 156, 302–314, 2006.

Zhang, Y. X.: H_2O in rhyolitic glasses and melts: measurement, speciation, solubility, and diffusion, Rev. Geophys., 37, 493–516, 1999.

SED
7, 3053–3085, 2015

Table 1. Normalised, average chemical analysis of Ramadas obsidian rocks from Gauthier (1994).

Oxides	Weight %
SiO_2	75.47
Al_2O_3	14.02
Na_2O	3.85
K_2O	4.78
MgO	0.01
CaO	0.56
TiO_2	0.01
FeO (T)	1.12
MnO	0.11
P_2O_5	0.05
Total	100.00

SED
7, 3053–3085, 2015

Table 2. Water content estimated by FTIR.

Sample	image	row	column	OH^-	Weight percents mol H_2O 1630 cm^{-1}	total H_2O 3500 cm^{-1}	Estimated magmatic H_2O
TPRT-1	A	4	48	0.88	4.34	5.22	1.19
TPRT-1	A	10	46	0.80	4.46	5.26	1.05
TPRT-1	A	18	50	0.68	4.87	5.55	0.85
TPRT-1	A	30	53	0.63	5.01	5.64	0.76
TPRT-1	A	39	55	0.65	4.74	5.39	0.80
TPRT-1	B	58	44	0.69	4.78	5.46	0.86
TPRT-1	B	2	33	0.72	4.74	5.46	0.92
TPRT-1	B	9	34	0.78	4.66	5.44	1.03
TPRT-1	B	47	41	0.79	4.90	5.69	1.04
TPRT-1	B	16	35	0.65	4.95	5.59	0.79
TPRT-1	C	22	25	0.82	4.81	5.64	1.09
TPRT-1	C	41	30	0.79	4.84	5.63	1.04
TPRT-1	C	55	35	0.72	4.78	5.49	0.91
TPRT-1	C	10	24	0.69	4.79	5.48	0.86
TPRT-1	C	26	30	0.59	4.93	5.52	0.69
TPRT-1	D	9	35	0.54	4.87	5.41	0.60
TPRT-1	D	18	43	0.72	4.84	5.55	0.91
TPRT-1	D	53	52	0.67	4.87	5.55	0.83
TPRT-1	D	30	43	0.66	4.89	5.55	0.81
TPRT-1	D	2	36	0.89	4.83	5.71	1.20
TPRT-1	E	11	32	0.66	4.89	5.55	0.81
TPRT-1	E	23	36	0.65	4.90	5.55	0.79
TPRT-1	E	37	33	0.23	4.97	5.21	0.08
TPRT-1	E	47	36	0.52	4.89	5.40	0.56
TPRT-1	E	59	38	0.78	4.62	5.39	1.01
AVERAGE				0.69	4.81	5.49	0.86

SED
7, 3053–3085, 2015

Table 2. Continued.

Sample	image	row	column	OH^-	Weight percents mol H_2O 1630 cm^{-1}	total H_2O 3500 cm^{-1}	Estimated magmatic H_2O
TPRT-2	A	28	20	0.92	3.72	4.64	1.26
TPRT-2	A	30	22	0.85	3.76	4.60	1.13
TPRT-2	A	23	32	0.92	3.59	4.51	1.26
TPRT-2	A	21	33	0.73	3.97	4.70	0.92
TPRT-2	A	21	21	0.79	4.08	4.87	1.03
TPRT-2	B	38	16	0.79	3.79	4.58	1.04
TPRT-2	B	34	11	0.78	4.07	4.85	1.02
TPRT-2	B	15	45	0.81	3.97	4.78	1.06
TPRT-2	B	8	52	0.96	3.90	4.86	1.32
TPRT-2	B	22	31	0.64	4.15	4.79	0.77
TPRT-2	B	18	38	0.67	3.46	4.13	0.83
TPRT-2	C	30	16	0.73	3.35	4.08	0.94
TPRT-2	C	26	24	0.81	4.10	4.91	1.07
TPRT-2	C	23	37	0.58	4.05	4.63	0.68
TPRT-2	C	16	51	0.63	3.94	4.56	0.75
TPRT-2	C	10	58	0.85	4.36	5.22	1.15
TPRT-2	D	31	10	0.80	4.02	4.82	1.05
TPRT-2	D	20	37	0.68	4.23	4.91	0.84
TPRT-2	D	12	52	0.81	4.13	4.94	1.06
TPRT-2	D	26	23	0.86	4.02	4.88	1.16
TPRT-2	D	19	41	0.69	4.20	4.89	0.86
TPRT-2	E	12	50	0.74	4.25	4.99	0.96
TPRT-2	E	15	45	0.78	4.18	4.96	1.02
TPRT-2	E	20	35	0.77	4.30	5.06	0.99
TPRT-2	E	17	44	0.68	4.28	4.96	0.85
TPRT-2	E	24	33	0.91	4.23	5.15	1.25
AVERAGE				0.78	4.00	4.78	1.01

SED
7, 3053–3085, 2015

Table 3. H and O isotope information.

Sample	$\partial^{18}O_{VSMOW}$ (‰)	∂D_{VSMOW} (‰)	H (wt. % H_2O)
JM RAM L (fresh)	14.0	−127	4.81
		−131	4.83
		−131	4.91
JM RAM W (weathered)	12.9	−135	5.06
	13.3	−133	5.07
		−136	4.89

SED
7, 3053–3085, 2015

Table 4. Bubble deformation and orientation for pure shear and simple shear scenarios as compiled by Rust et al. (2003) and reference therein. a, c, l are the semi-principal axes of the deformed bubbles (see Fig. 8a). $D = (l - b)/(l + b)$.

Geometrical conditions	Pure shear	Simple shear
Bubble deformation: $Ca \ll 1$	$D = 2Ca$	$D = Ca$
Bubble deformation: $l/a \gg 1$	$l/a = 16Ca^{2*}$	$l/a = 3.45Ca^{1/2}$
Bubble orientation: $Ca \ll 1$	$\theta = 0$	
Bubble orientation: $l/a \gg 1$	$\theta = 0$	$\theta = \tan^{-1}(0.359Ca^{-3/4})$

* The constant of proportionality in the bubble deformation equation for. $l/a \gg 1$ assumes that $P/G\mu_s = 2$, where P is the pressure in the bubble.

SED
7, 3053–3085, 2015

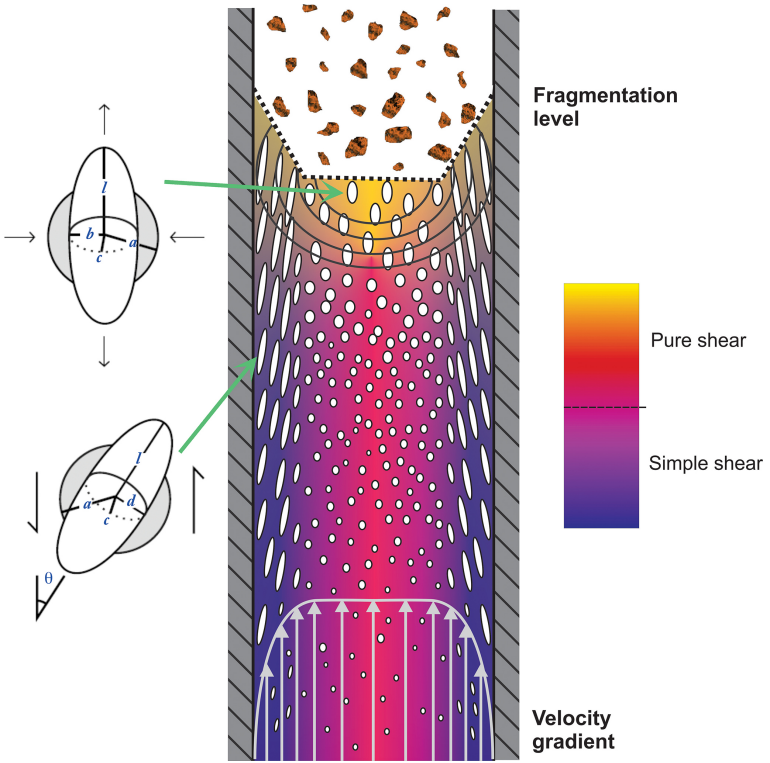

Figure 1. Eruptive shearing. A Schematic view of magma shearing during eruptions. Strain localisation along the conduit margins promotes a heterogeneous velocity gradient, which induces simple shearing (blue) and stretching of bubbles (white ellipses). In the core of the magma column, a relatively low velocity gradient leaves the bubbles mostly undisturbed and near isotropic. Relatively rapid decompression increases bubble pressure, which, if exceeding the magmastatic pressure, will force the bubbles into a tensional regime, which may promote pure shear. The deformed bubble shape can be characterised by the semi-principle axes of a best-fit ellipsoid *l*, *b*, and *c* (modified from Rust et al., 2003).

SED
7, 3053–3085, 2015

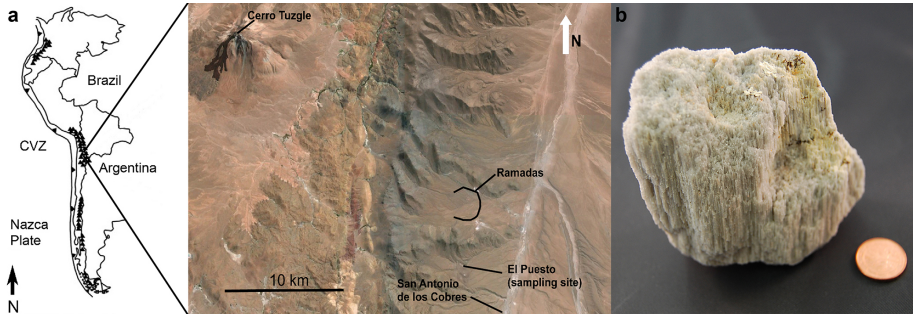

Figure 2. (a) Location of the Ramadas Volcanic Complex (RVC) in the Altiplano-Puna Plateau, Argentina. **(b)** Photograph of a tube pumice from the Ramadas fallout deposit. Coin as scale: 20 mm diameter.

SED
7, 3053–3085, 2015

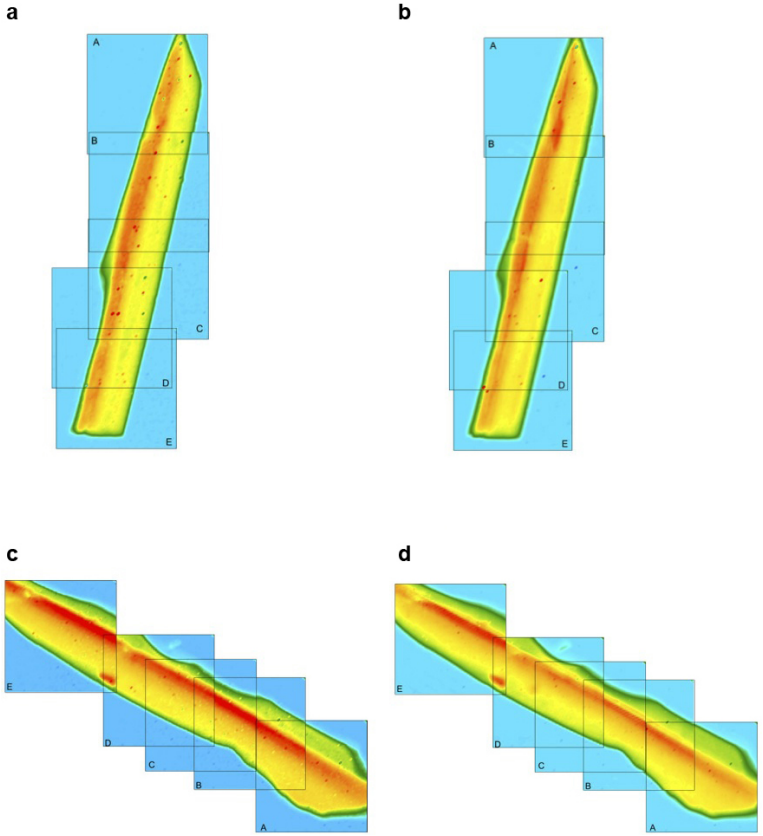

Figure 3. Water distribution in two bubble wall fragments: **(a–b)** TPRT1 and **(c–d)** TPRT2. **(a, c)** show absorbance of the 3567 cm^{-1} band, and **(b, d)** absorbance of the 1628 cm^{-1} band. The composite reconstruction is made of FTIR images of 350 µm × 350 µm (for each box).

SED
7, 3053–3085, 2015

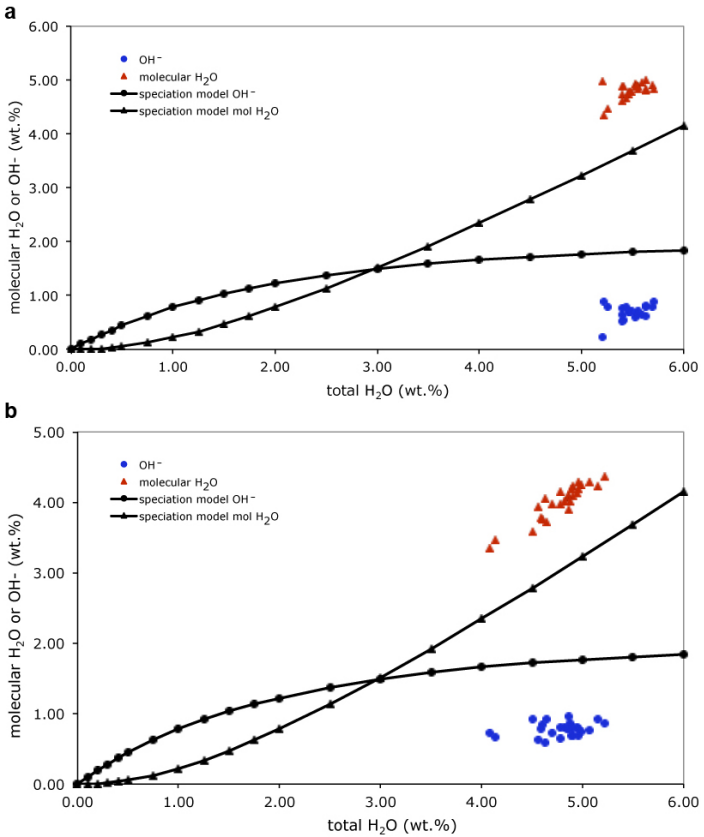

Figure 4. Speciation of water for bubble wall samples **(a)** TPRT1 and **(b)** TPRT2, plotted against the equilibrium speciation model for rhyolites of Zhang (1999).

SED
7, 3053–3085, 2015

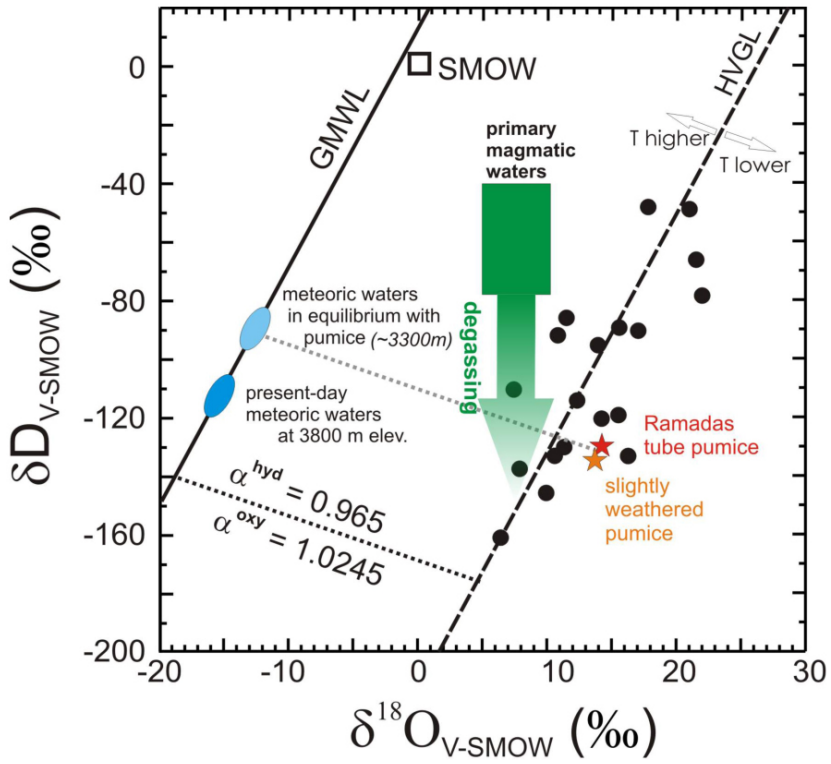

Figure 5. Oxygen and hydrogen isotope composition of tube pumice (stars; red: fresh glass, orange: weathered sample), meteoric waters in equilibrium with the glasses, and present-day local meteoric waters. Primary Magmatic Waters from Sheppard et al. (1969), Degassing trend (green arrow) from Taylor et al. (1983), HVGL: hydrated volcanic glass line from Taylor (1968), black dots: hydrated silicic volcanic glasses from Taylor (1968), Cerling et al. (1985) and Compton et al. (1999); SMOW: Standard Mean Ocean Water; GMWL: Global Meteoric Water Line.

SED
7, 3053–3085, 2015

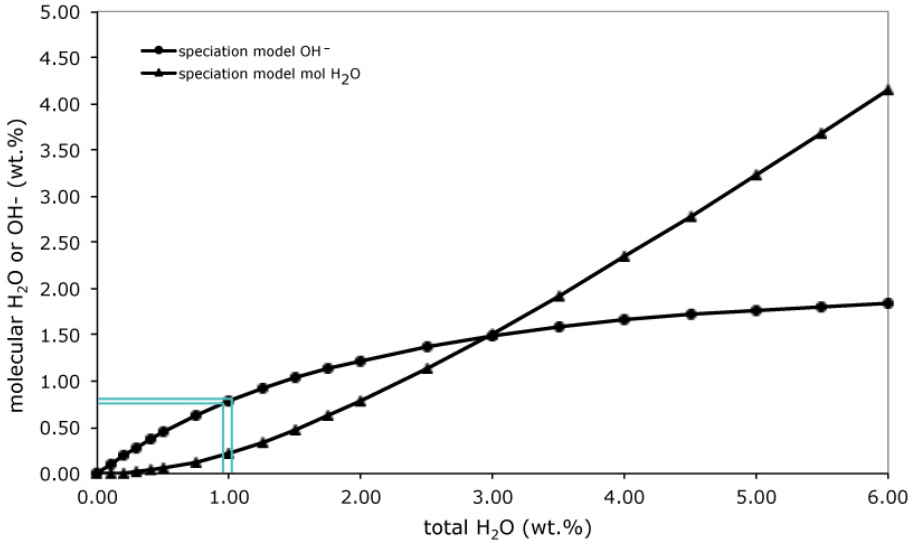

Figure 6. Total magmatic water extrapolated from the OH^- concentrations measured by FTIR using the equilibrium speciation model for rhyolites of Zhang (1999).

SED
7, 3053–3085, 2015

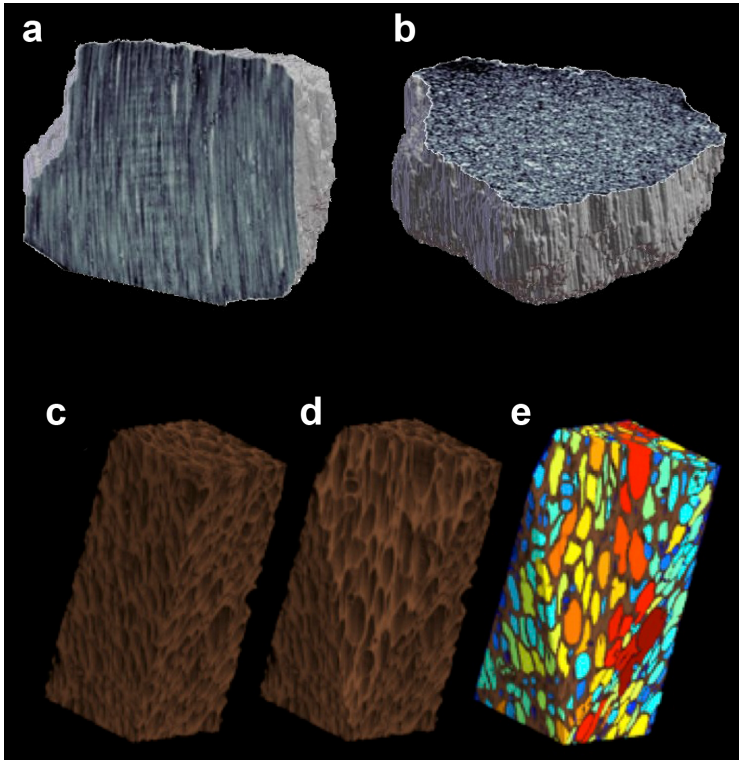

Figure 7. NCT reconstruction of the tube pumice showing the internal structure of the tubular texture **(a)** in parallel and **(b)** perpendicular cross sections. **(c)** Rendering of a sub-volume taken from the tube pumice NCT. **(d)** Cut away of the rendering shown in **(c)**, revealing some of the internal structure of the sub-volume **(e)** A false-colour composite showing the result of the segmentation algorithm. Here each pore has been colour coded based on its volume, with small pores shaded blue increasing through the colour spectrum to large pores, which are shaded red; voxel size is 51.2 µm × 51.2 µm × 51.2 µm (i.e., about 7 mm^3).

SED
7, 3053–3085, 2015

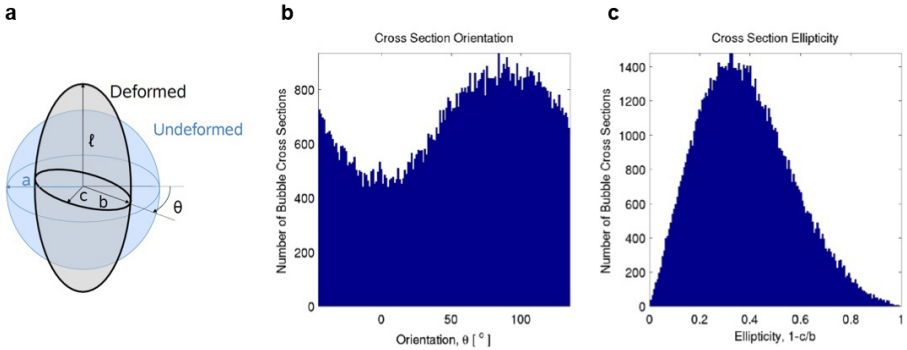

Figure 8. Parametrisation of pores. **(a)** Geometry used to parameterise the pores. Distribution of the frequency of pores identified with **(b)** different orientation and **(c)** ellipticity.

SED
7, 3053–3085, 2015

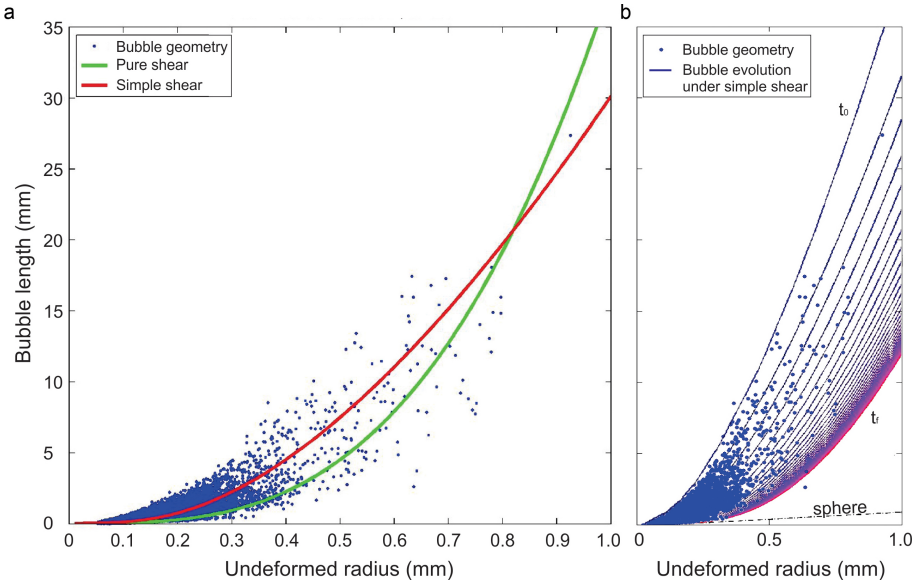

Figure 9. Bubble geometry population and shear models. Bubble geometry distribution compared to **(a)** the best fit for simple (red) and pure shear (green). **(b)** The best fit for simple shear requires a characteristic cooling rate of $10^{-4.9}\,s^{-1}$ and a strain rate of $10^{-2}\,s^{-1}$. Applying a cooling rate profile across the sample explains the data distribution. The best fit for pure shear requires a non-physical, infinitely fast, cooling rate; a realistic cooling rate pushes the modelled bubble length to below the imaged population, rejecting the possibility that pure shear induced the porous structure of the tube pumice.

SED
7, 3053–3085, 2015